# <sup>6</sup>A Method to Quantify Bedform Height and Asymmetry from a Low-Mounted Sidescan Sonar

### KATIE R. JONES

Massachusetts Institute of Technology–Woods Hole Oceanographic Institution Joint Program, Cambridge, and Department of Applied Ocean Physics and Engineering, Woods Hole Oceanographic Institution, Woods Hole, Massachusetts

#### PETER TRAYKOVSKI

Department of Applied Ocean Physics and Engineering, Woods Hole Oceanographic Institution, Woods Hole, Massachusetts

(Manuscript received 5 June 2017, in final form 1 March 2018)

### ABSTRACT

Rotary sidescan sonars are widely used to image the seabed given their high temporal and spatial resolution. This high resolution is necessary to resolve bedform dynamics and evolution; however, sidescan sonars do not directly measure bathymetry, limiting their utility. When sidescan sonars are mounted close to the seabed, bedforms may create acoustical "shadows" that render previous methods that invert the backscatter intensity to estimate bathymetry and are based on the assumption of a fully insonified seabed ineffective. This is especially true in coastal regions, where bedforms are common features whose large height relative to the water depth may significantly influence the surrounding flow. A method is described that utilizes sonar shadows to estimate bedform height and asymmetry. The method accounts for the periodic structure of bedform fields and the projection of the shadows onto adjacent bedforms. It is validated with bathymetric observations of wave-orbital ripples, with wavelengths ranging from 0.3 to 0.8 m, and tidally reversing megaripples, with wavelengths from 5 to 8 m. In both cases, bathymetric-measuring sonars were deployed in addition to a rotary sidescan sonar to provide a ground truth; however, the bathymetric sonars typically measure different and smaller areas than the rotary sidescan sonar. The shadow-based method and bathymetric-measuring sonar data produce estimates of bedform height that agree by 34.0% ± 27.2% for wave-orbital ripples and  $16.6\% \pm 14.7\%$  for megaripples. Errors for estimates of asymmetry are  $1.9\% \pm 2.1\%$ for wave-orbital ripples and  $11.2\% \pm 9.6\%$  for megaripples.

### 1. Introduction

The ability of subaqueous bedforms to steer flow, influence seabed friction, and affect the transport of sediment makes observing bedforms crucial to understanding coastal systems. Bedforms have been observed from a variety of platforms (ship-based and underwater frames) and instruments (optical and acoustical). To document bedform dynamics and evolution, both high temporal and spatial resolution data are required. Ship-based

Oenotes content that is immediately available upon publication as open access.

Corresponding author: Katie R. Jones, ksamuel@mit.edu

measurements with modern multibeam sonars can provide a spatial resolution of approximately 10 cm when taken in shallow waters ( $\sim 10 \,\mathrm{m}$ ). This is sufficient to measure bedforms on the order of 1 m or larger; however, it is difficult to capture smaller bedforms. Ship-based measurements are also limited temporally, as repeated surveys are difficult and expensive, especially on short tidal time scales or during storm events. To address these limitations, sidescan sonars have been mounted on underwater frames and rotated 360° to obtain a circular image of the backscattered intensity of the seafloor (such instruments are referred to as rotary sidescan sonars; Irish et al. 1999; Hay and Wilson 1994; Rubin et al. 1983). Unlike the 10-cm resolution of multibeam sonars, rotary sidescan sonars can have a 2-cm resolution over a  $40\,\mathrm{m} \times$ 40 m area and at very high-temporal (minutes to hourly)

resolution. Because of their ability to consistently survey the same area over long periods of time, studies with rotary sidescan sonars are able to resolve temporal bedform dynamics.

Although sidescan sonars provide an image of the seafloor, they are unable to obtain direct measurements of seafloor elevation. Recent developments in image processing have enabled backscatter intensity to be inverted to obtain seabed elevation maps using an image model based on surface roughness scattering strength (Coiras et al. 2007; Tang et al. 2009; Nishimura 1997). In nearshore environments, where the water is shallow and bedforms are ubiquitous as a result of ample sediment supply, waves, and currents, sensors are often mounted close to the bed. Given these shallow depths and low grazing angles, shadows form away from the sonar as bedforms block the acoustic waves from reaching the seafloor behind them (Blondel 2009; Reed et al. 2003). Except for a very limited area below the sonar that does not contain shadows, the backscatter intensity inversion methods become ineffective, as they are based on an assumption of full insonification of the seabed. This is especially problematic with larger bedforms ( $\lambda > 1$  m; see Table 1 for definitions of symbols), as only one or two bedforms may be present in the nonshadowed area, leading to poor statistical estimates.

Previous efforts have revealed methods to estimate object heights, such as mines, from sidescan sonar shadows; however, these methods typically assume a flat seabed with uninterrupted shadows (Reed et al. 2003; Doherty et al. 1989; Chew et al. 2007). This flat seabed assumption is not applicable to estimating bedform height, as bedforms typically occur in sets where the shadow cast from one bedform is truncated by the subsequent bedform. This shortening of the shadow length reduces the apparent bedform height. Previous work has been conducted on estimating bedform heights from sidescan shadows; however, most of this work provides limited details and assumptions on how these estimates were obtained (Bouma et al. 1980; Green 1986). In Lonsdale et al. (1972) a cross profile of the bedforms suggests a triangular geometry was used in estimating dune height from shadows where the lee slope was additionally estimated from the maximum slope of the shadowed ray. Depending on the horizontal location of the bedform relative to the sonar, the lee slope may be underestimated when using the maximum shadowed ray slope as the lee slope.

This paper contributes to this body of knowledge by utilizing sidescan acoustic shadows to explicitly and directly estimate bedform height and asymmetry, validating this method against independently measured bedform parameters, and providing sensitivity analyses

TABLE 1. Table of symbols.

В	Length of bright return
c	Horizontal distance from crest to trough of a bedform
$d_{50}$	Median grain diameter
h	Bedform height
$H_i$	Sonar height
l	Reference to geometry to the left of the sonar
L	Distance from sonar to start of shadow
m	Ray slope
r	Reference to geometry to the right of the sonar
R	Slant distance from sonar
S	Length of shadow
$x_{\rm crit}$	Critical distance from sonar for sinusoidal bedforms
$x_{\text{sonar}}$	Maximum range of the sonar
X	Horizontal distance from sonar
$X_L$	Nondimensional critical distance for sinusoidal bedforms
y	Height shadow intercepts subsequent bedform
z	Seabed elevation
$\alpha$	Bedform asymmetry
β	Coefficients for empirical models of error
γ	Coefficient for recommended sonar height from seabed
λ	Bedform wavelength

Angle of seabed for scour pit

on the assumptions made. First, we describe the geometric model used to derive the method, assuming triangular bedforms on a flat seabed and known horizontal range. We then discuss the effects of realistic variability, including crest sharpness, a sloping seabed caused by scour, and approximating the horizontal range given the assumption that the sonar is mounted significantly higher than the seabed perturbations. Theoretical bedform fields are generated that incorporate this variability and the error computed when assuming the simplified idealized bedform configuration. Empirical models are fit to the error and used to correct for the variability. Sensitivity analyses are also performed on the assumption of uniform parameters. The method is then validated with field data in which both sidescan sonar images and bathymetry are obtained. This validation took place in locations with wave-orbital ripples and tidally reversing bedforms, features that do not scale with water depth like dunes, but are larger than typical ripples, to demonstrate the performance of the method on different types of bedforms.

# 2. Geometric model

# a. System geometry

Rotary sidescan sonars transmit a fan of acoustic waves and record the intensity of the reflected, or backscattered, returns (Klein 2002, 667–678). The location of this intensity is recorded in units of "range" distance, based on the time it takes an echo to leave the

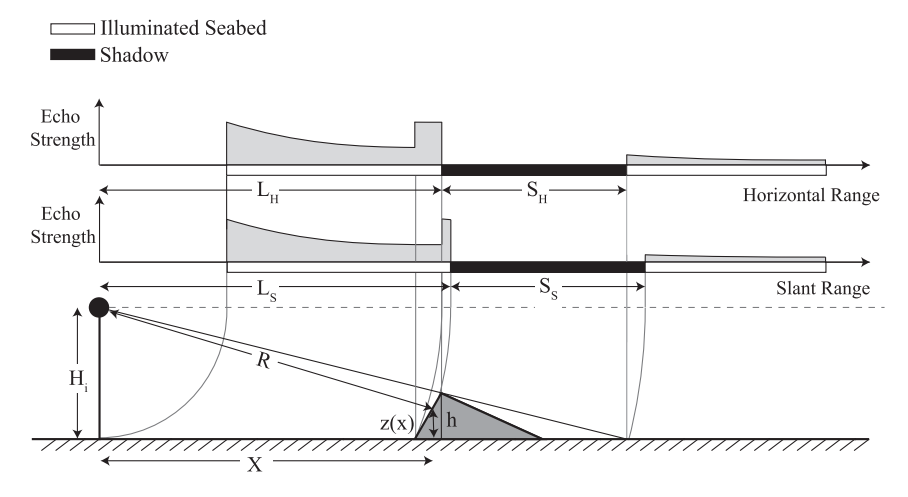


FIG. 1. System geometry and backscattered intensity of a flat seabed with a single bedform present. The difference between horizontal and slant ranges is depicted in the system geometry as well as the echo return strength. The horizontal range, or horizontal distance from the sonar to an arbitrary location, is denoted as X while the slant range to this same location is represented by R and is a function of X, the height of the sonar,  $H_i$ , and the height of the seabed at the location of interest, z(x). The difference in backscatter intensity of slant and horizontal ranges is depicted in the plots of range vs returned echo strength. In these plots, S is the length of the shadow caused from the bedform intercepting the acoustic wave and L is the distance from the sonar to the start of the shadow. The subscripts indicate whether these distances were obtained using the horizontal (subscript H) or slant (subscript S) range.

transducer, hit a target, and return to the sonar. The distance from the transducer to the target is the "slant" range, R (Fig. 1). Therefore, objects at the same range but different elevations will be recorded at the same location. If the seabed bathymetry, z(x), is known, the horizontal range, X, can be computed from the slant range given the height of the sonar from the seabed,  $H_i$ :

$$X = \sqrt{R^2 - [H_i - z(x)]^2}.$$
 (1)

However, because rotary sidescan sonars are imaging sonars that provide only backscatter intensity not depth, the seabed elevation, z(x) is usually unknown. By assuming the sonar is mounted significantly higher than the elevation of seabed perturbations  $[H_i \gg z(x)]$ , or that the range is much larger than the sonar height  $(R \gg H_i)$ , Eq. (1) can be simplified as

$$X = \sqrt{R^2 - H_i^2} \tag{2}$$

in which the horizontal range, X is no longer a function of z(x) and will therefore be referred to as the "depth independent range" for the remainder of the paper. This approximation is valid for most instrument deployments and will be used to compute the horizontal range needed in the method described below. The sensitivity of the method to this assumption is discussed in section 3c.

### b. Single triangular bedform

As demonstrated in existing literature (Reed et al. 2003; Doherty et al. 1989; Chew et al. 2007), the height of a single object on a flat seabed can be explicitly determined from the geometry of the system. Although the height can be computed when there is one bedform present on a flat seabed, the bedform asymmetry cannot be determined. Given the height of the sonar,  $H_i$ , the distance of the object from the sonar, L, and the length of the shadow, S, the height can be explicitly determined (Fig. 1) using

$$\frac{H_i}{L+S} = \frac{h}{S}. (3)$$

This holds true for both the horizontal range measurements ( $L_H$  and  $S_H$ ) and the slant range measurements ( $L_S$  and  $S_S$ ) as depicted in Fig. 1.

# c. Multiple triangular bedforms

It is unlikely for a single bedform to exist on a flat seabed given feedbacks between bottom perturbations, the movable seabed, and the overlying flow. Because of its influence on the flow, a single bedform will decrease the bed shear stress downstream of the bedform, resulting in the downstream deposition of sediment, and the generation of a secondary bedform (Bagnold 1946; Dalrymple and Rhodes 1995). As this process repeats

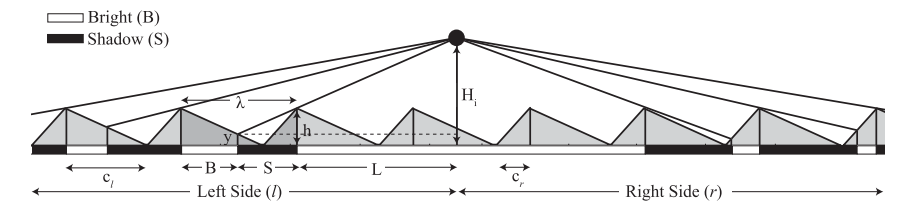


FIG. 2. Geometry to determine bedform height (h) and asymmetry ( $\alpha$ ) when multiple triangular bedforms are present. The same notation is used as in Fig. 1 with additional parameters being defined as the wavelength ( $\lambda$ ), the distance between the bedform trough and the crest facing the sonar (c), and the height on the adjacent ripple where the shadow intersects (y). The length of c facing the sonar varies depending on the side of the sonar considered where  $c_r$  is the length of the base facing the sonar on the right side of the sonar and  $c_l$  is the length of the base facing the left side of the sonar.

itself, a field of bedforms form, and the lengths of bedform shadows become intercepted and shortened by subsequent bedforms (Fig. 2) invalidating Eq. (3). By assuming a field of uniform triangular bedforms on a flat seabed, individual bedform heights and asymmetries can be determined. Similar to the single-bedform case, the geometry of the system is used to obtain a relationship between the bedform shape and the shadow pattern:

$$\frac{H_i - y}{L + S} = \frac{h - y}{S},\tag{4}$$

where  $y = h(c - B)c^{-1}$  is the height at which the shadow intercepts the subsequent bedform,  $B = \lambda - S$  is the length of brightness or strong return, and c is the horizontal distance from the bedform crest to the trough, closest to the sonar (Fig. 2). Because  $\lambda$  and c are defined based on horizontal distances, the quantities L, S, and Bare computed using the horizontal depth independent range in Eq. (2) as opposed to the slant range. Also, while S and B are directly related to one another given a uniform wavelength, both measurements are maintained throughout the paper, as the assumption of a uniform wavelength is not always true, especially for field data. It is therefore recommended that users compute B directly from the length of the bright return of the sonar. Simplifying Eq. (4) and substituting the expression for y, we relate the shadow pattern directly to the bedform height and c, which is a measure of bedform asymmetry:

$$\frac{h}{(H_i - h)c} = \frac{S}{BL}. (5)$$

When there are multiple bedforms, Eq. (5) becomes a system of equations with two unknowns for each bedform: h and c. If at least two bedforms are present such that there are two measurements of S, B, and L the height and c can be directly computed given the two equations

and two unknowns; however, variability in the field data results in poor estimates with only two bedforms.

The estimates can be improved for asymmetric bedforms if the shadow pattern is obtained on each side of the sonar as one face of the bedform is illuminated on one side of the sonar while the other face of the bedform is illuminated on the other side of the sonar. This results in a different shadow pattern on each side. On the right (r) side of the sonar Eq. (5) becomes  $h/[(H_i - h)c_r] = S_r/(B_rL_r)$ , and on the left (l) side of the sonar it becomes  $h/[(H_i - h)c_l] = S_l/(B_lL_l)$ . Defining the geometry based on each side of the sonar as opposed to flow direction is necessary to quantify bedform reversal in tidal flows where the lee and stoss sides change as the definition of downstream changes.

By assuming that all bedforms have the same height and asymmetry, Eq. (5) for each side can be combined into a single equation relating the lengths of the two bedform bases to the shadow pattern:

$$\frac{c_r}{c_l} = \frac{B_r L_r}{S_r} \frac{S_l}{B_l L_l}.$$
 (6)

Because  $c_r + c_l = \lambda$ , Eq. (6) can be simplified further and written in terms of an asymmetry parameter,  $\alpha = c_r/\lambda$ , that ranges from 0 to 1 with symmetric bedforms having  $\alpha = 0.5$ . This parameter is similar to the asymmetry parameter defined by Clifton and Dingler (1984), Lefebvre et al. (2016), and Haque and Mahmood (1985); however, instead of defining the asymmetry as  $\beta/\lambda$  (here  $\beta$  is the downstream distance from crest to trough),  $\alpha$  is defined based on a prescribed direction to permit the quantification of bedform orientation reversals:

$$\alpha = \frac{c_r}{\lambda} = \frac{\lambda - c_l}{\lambda} = \frac{\frac{B_r L_r}{S_r}}{\frac{B_r L_r}{S_r} + \frac{B_l L_l}{S_l}}.$$
 (7)

The bedform shadow length, S, brightness length, B, and distance from sonar, L, are obtained for each bedform from the rotary sidescan sonar imagery as discussed in section 4b. By assuming that all bedforms have the same height and shape, the ratio S/(BL) is the same for the bedforms on each side of the sonar [Eq. (5)]. Therefore, for a field of uniform triangular bedforms on a flat bed, bedform asymmetry can be estimated if at least one bedform exists on each side of the sonar; this bedform casts a shadow, and the end of that shadow is also captured by the sonar. If shadow information exists for more than one bedform on each side, then there are multiple estimates for S/(BL). To get a single estimate of  $\alpha$ , it is necessary to combine the estimates. We have chosen to use the median as our measure of central tendency because it is robust to outliers.

After computing bedform asymmetry, the height of each bedform can be estimated by solving Eq. (5) for h; however, separate equations are required for each side of the sonar when the bedforms are asymmetric, as each side has a different value for c [Eqs. (8) and (9)]:

$$h_r = \frac{H_i}{\frac{B_r L_r}{S_r(\alpha \lambda)} + 1},\tag{8}$$

$$h_l = \frac{H_i}{\frac{B_l L_l}{S_l [(1 - \alpha)\lambda]} + 1}.$$
 (9)

### 3. Error correction and sensitivity analysis

In the idealized case of theoretical triangular bedforms on a flat seabed with a known horizontal range, the estimated bedform height and asymmetry from Eqs. (7), (8), and (9) agree with the true prescribed values. However, a flat seabed of uniform triangular bedforms is not realistic. An empirical error correction was obtained for three realistic variations: crest sharpness, a scoured seabed, and approximating the horizontal range as the depth independent range. For each variation, a theoretical bedform field based on realistic parameters was generated, and the height and asymmetry computed. The error was obtained given this estimated parameter and the true parameter. An empirical model was then fit to the error to be applied after estimating the parameters as a correction to the variability. Each variability component was considered individually with the interaction of all variability configurations addressed in section 3d.

Additionally, a sensitivity analysis of the assumption of a uniform bedform field was performed by theoretically prescribing a distribution of bedform parameters and computing the error in estimated height and asymmetry. First, normal distributions of bedform height and wavelength were applied to otherwise uniform triangular bedforms on a flat seabed to test the sensitivity of the method to slight variations in individual bedforms. Second, a bimodal distribution of bedform parameters was considered in which smaller bedforms were superimposed on top of larger bedforms of the same aspect ratio.

For readers who seek to apply the method, proceed to section 4. The below subsections detail the incorporation of variability and the generation of the empirical error models.

### a. Crest sharpness

While bedforms are approximately triangular, they typically have some curvature associated with a rounded trough and crest (Dalrymple and Rhodes 1995; Lefebvre et al. 2016). A number of laboratory and numerical studies assume a sinusoidal stoss side and a straight lee side to approximate current-generated bedforms (Lefebvre et al. 2016; Smith and McLean 1977; Nelson et al. 1993). For the generality of tidally reversing and symmetrical bedforms, we will account for this curvature by assuming both sides of the bedform are sinusoidal (Fig. 3).

A field of uniform sinusoidal bedforms results in the same relationship between bedform shape, distance from the sonar, and shadow lengths as for the field of triangular bedforms [Eq. (4)]. However, the height at which the shadow intercepts the following bedform, y, is defined based on the sinusoidal shape:

$$y = \frac{h}{2}\cos\left(\frac{B\pi}{c}\right) + \frac{h}{2}.\tag{10}$$

Substituting this equation for y into Eq. (4) results in the following equation for the bedform height and c with respect to the measured distance from sonar and shadow length:

$$\frac{H_i - h}{h} = \frac{L}{2S} \left( 1 - \cos \frac{B\pi}{c} \right) \tag{11}$$

Similar to the case for a field of triangular bedforms, Eq. (11) has two unknowns—h and c—for each bedform. To overcome the poorly constrained case of triangular bedforms, both sides of the sonar are considered separately, as the ratio of BL/S is constant for all bedforms on each side. In the case of sinusoidal bedforms [Eq. (11)], it is not possible to partition the unknowns (c and h) from the knowns (B, L, S), which is necessary when considering each side of the sonar separately. Thus, we assume triangular bedforms and quantify the error resulting from reduced crest sharpness, which is common in current-generated bedforms or high flow wave-generated ripples (Nielsen 1992).

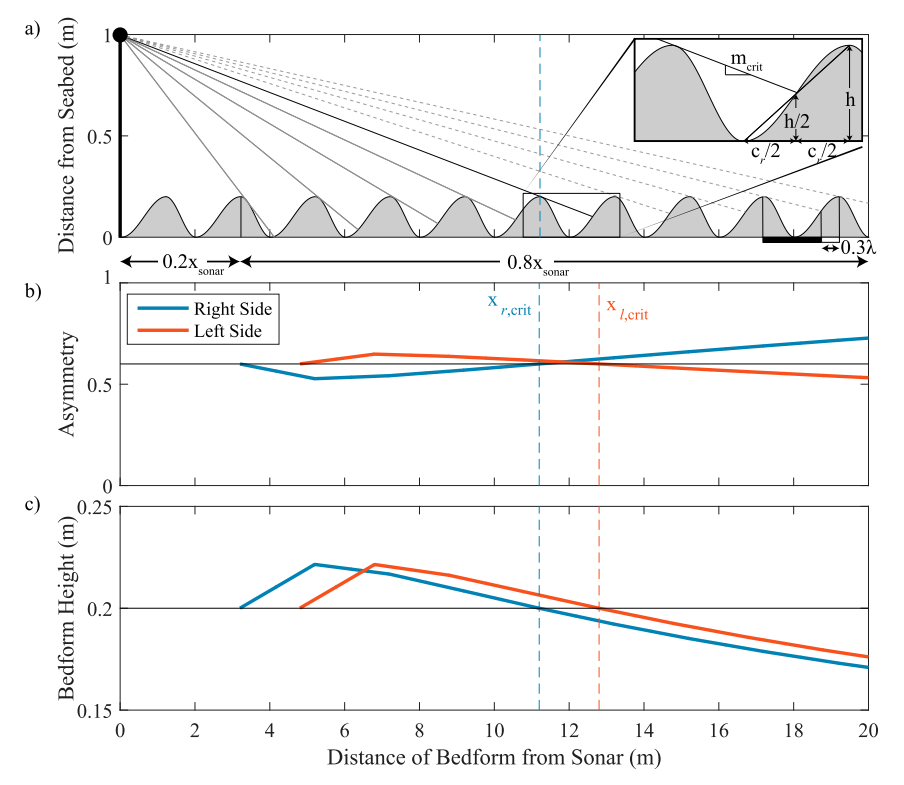


FIG. 3. (a) System geometry for the right side of the sonar, where bedforms are the composite of two sine waves. In this example, the sonar is 1 m above the seabed, and bedforms have a wavelength of 2 m, a height of 0.2 m, and an asymmetry of 0.6. Ray traces from the sonar to the bedform crests are shown where rays are  $m > m_{\rm crit}$  (solid gray lines) and  $m < m_{\rm crit}$  (dashed gray lines). The critical ray (solid black ray) is where asymmetry and height are accurately estimated. The annotations underneath the subplot are for reference when computing the recommended sonar height in section 4a. (b) Estimated asymmetry for the left and right sides as a function of distance from the sonar. The asymmetry equals the true asymmetry of 0.6 at the critical length (vertical dashed lines). (c) Estimated height assuming triangular bedforms for each side of the sonar. For distances shorter than the critical length, the height is overestimated, while distances larger than the critical length, the height is underestimated.

A sinusoidal bedform will result in either a larger or smaller shadow depending on the location at which the ray intercepts the subsequent bedform. At the inflection point of a sinusoidal curve, the height and location of a sinusoidal bedform is the same as that of a triangular bedform (Fig. 3a). The slope of the ray from the sonar to this point will be referred to as the critical slope and is defined as

$$m_{\rm crit} = \frac{h/2}{\lambda - c/2}.\tag{12}$$

The shadows lengths are longer for sinusoidal bedforms than triangular bedforms when the slope of a given ray,  $m = (H_i - h)/L$ , is larger than the critical slope [Eq. (12); and indicated in Fig. 3a by the solid gray lines]. Thus, c is underestimated by Eq. (5) on both sides of the sonar, and the asymmetry will be underestimated for the right side ( $\alpha = c_r/\lambda$ ) and overpredicted for the left side  $[\alpha = (\lambda - c_l)/\lambda;$  Fig. 3b]. However, as the slope of the ray becomes smaller than the critical slope (indicated by the dashed gray lines in Fig. 3a), the observed shadow lengths are shorter than if the bedform was triangular, overestimating c on both sides as well as overestimating c on the right side and underestimating c on the left side (Fig. 3b).

Sinusoidal bedforms also influence the estimated bedform height as a function of the ray slope and critical slope. If the shadow lengths are increased such that the ray slope is larger than the critical slope, then the ratio of BL/S is underestimated, producing an overestimate of h. Likewise, if the shadow lengths are decreased, which occurs when the ray slope is smaller than the critical slope, then the ratio of BL/S is overestimated, resulting in an underestimate of the bedform height (Fig. 3c).

Whether the overall estimated height and asymmetry are over- or underpredicted depends on how many

TABLE 2. Range of parameters used in theoretical system geometries to obtain empirical models of the error in estimated height and asymmetry.

Parameter	Range
α	[0: 1]
λ	[0.5 m: 6 m]
h	$[0.05\lambda:0.2\lambda]$
$H_i$	$[0.05\lambda:2.5\lambda]$
$\chi_{ m sonar}$	[10 m: 20 m]

bedforms have a ray slope less than or greater than the critical slope. Because a central tendency, such a mean or median, is computed for each side, the error will depend on the ray slope relative to the critical slope. The error as a function of slope can also be described in terms of length, where the length is defined as  $x = (H_i - h)/m$ . Therefore, if the average ratio of BL/S is obtained from each side, the error in estimated height and asymmetry will depend on the number of bedforms that occur at a distance smaller than  $x_{\rm crit}$  as well as the number of bedforms that occur at a distance larger than  $x_{\rm crit}$ .

The error in estimated height and asymmetry from applying Eqs. (7)–(9) (assuming triangular bedforms)

was quantified on theoretical sinusoidal bedforms. The shape and size of the theoretical bedforms, along with the system geometry, were randomly generated for  $10^5$  sets of realistic parameters of  $\alpha$ ,  $\lambda$ , h,  $H_i$ , and the maximum range of the sonar,  $x_{\rm sonar}$ . The range of these parameters randomly selected for each configuration are shown in Table 2. The difference in estimated asymmetry and true asymmetry ( $\alpha_{\rm est} - \alpha_{\rm true}$ ) for each realization is shown in Fig. 4a, and the error in height  $[(h_{\rm est} - h_{\rm true})/h_{\rm true}]$  is shown in Fig. 4b.

An empirical model was fit to the error using multiple linear regression with both interaction and nonlinear transformation predictors. The empirical model for error in asymmetry can be represented by Eq. (13) and has an  $R^2$  of 0.77. All coefficients were significant with a p value less than 0.001 and are given in Table 3. In the model  $X_L = x_{\text{critavg}}/x_{\text{sonar}}$ , where  $x_{\text{critavg}}$  is the average critical length for the right and left sides. The critical length,  $x_{\text{crit}}$ , varies for each side for asymmetric bedforms (Fig. 3); however, their average provides a good indication of over- and underestimation of asymmetry and height, and can be simplified such that  $X_L = 1.5(H_i \lambda h^{-1} - \lambda) x_{\text{sonar}}^{-1}$ 

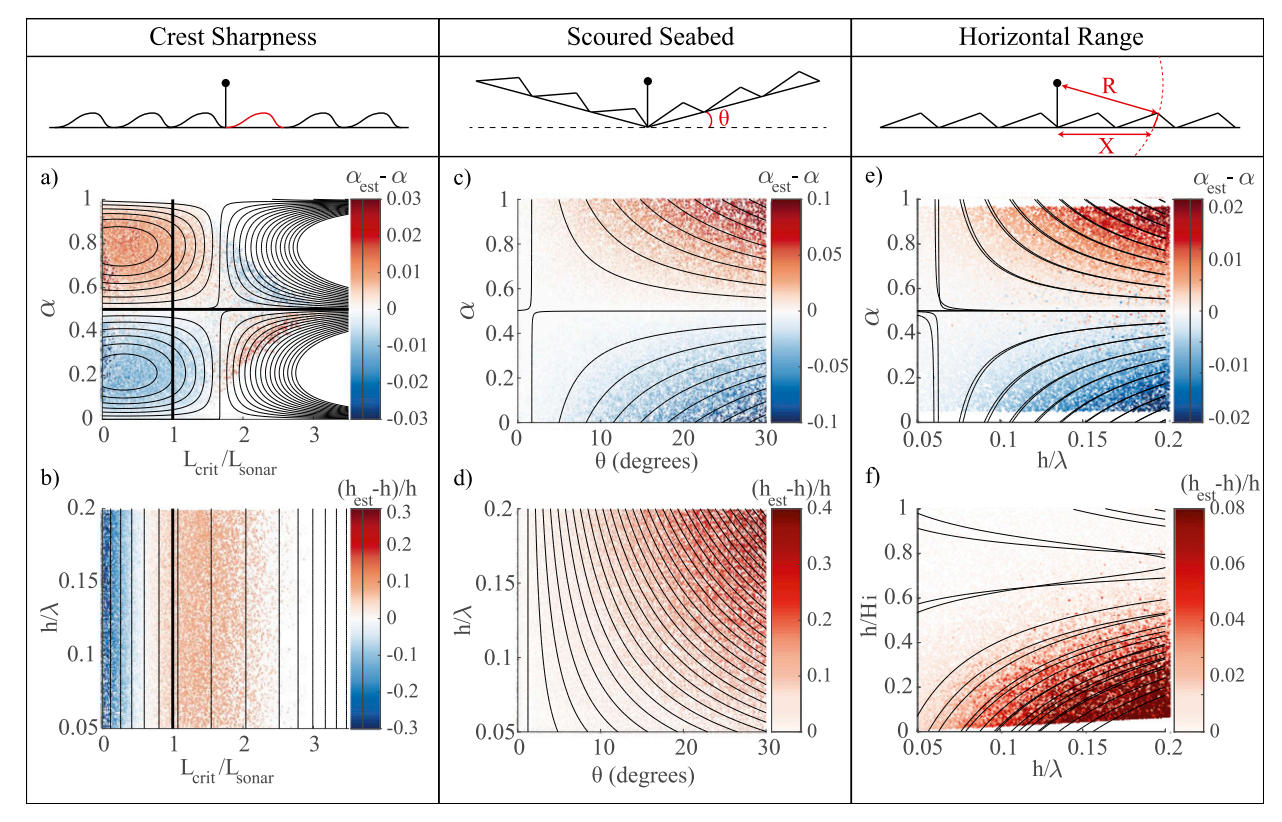


FIG. 4. Scatterplots of error from theoretical bedforms. Contours are the empirically fitted models. (top) The error in asymmetry and (bottom) the error in height. (a),(b) Error introduced from assuming sinusoidal bedforms are triangular. (c),(d) Error from having a constant-sloped, scoured seabed. (e),(f) Error from approximating the horizontal range as the depth independent range.

TABLE 3. Empirical model coefficients for quantifying the error in asymmetry given sinusoidal bedforms.

Coefficients	Estimate	Standard error
$\beta_0$	-0.135	0.001
$oldsymbol{eta}_1$	0.405	0.003
$oldsymbol{eta}_2$	-0.269	0.002
$\beta_3$	-0.046	0.002
$eta_4$	0.139	0.007
$eta_5$	-0.095	0.005
$\beta_6$	0.076	0.001
$oldsymbol{eta_7}$	-0.229	0.004
$oldsymbol{eta}_8$	0.154	0.003

$$\alpha_{\text{est}} - \alpha = \beta_0 \alpha + \beta_1 \alpha^2 + \beta_2 \alpha^3 + \beta_3 \alpha X_L + \beta_4 \alpha^2 X_L + \beta_5 \alpha^3 X_L + \beta_6 \alpha X_L^2 + \beta_7 \alpha^2 X_L^2 + \beta_8 \alpha^3 X_L^2.$$
(13)

A similar empirical model was also fit for the error in height given the nondimensional critical length,  $X_L$  [Eq. (14)]. The model has an  $R^2$  of 0.90, and all coefficients (shown in Table 4) are significant with a p value less than 0.001,

$$\frac{h_{\text{est}} - h}{h} = \beta_0 + \beta_1 X_L + \beta_2 X_L^2. \tag{14}$$

The empirical equations for error in height and asymmetry can be used to correct for the assumption of triangular bedforms by solving Eqs. (13) and (14) for  $\alpha$  and h, respectively, and substituting  $X_L$  and the estimated parameters. The term  $X_L$  is a function of the unknown h in Eq. (13). Therefore, the height can be corrected by first solving for h in Eq. (14) and this empirically corrected height used in  $X_L$  to then correct for the asymmetry using Eq. (13).

#### b. Scoured seabed

Rotary sidescan sonars are usually mounted on an underwater frame in order to observe bedform dynamics. The interaction of the frame with the flow and movable seabed can result in a scour pit around the frame (Bolaños et al. 2011). If substantial scouring has occurred, the angle of the seabed relative to the sonar will be decreased, affecting the estimated asymmetry and height of the bedform. To determine these effects, the system geometry parameters  $(\alpha, \lambda, h, H_i, \text{ and } x_{\text{sonar}})$ were randomly generated for 10<sup>5</sup> configurations, in which the seabed slope  $(\theta)$  was varied from  $0^{\circ}$  to  $30^{\circ}$  to approximate the effects of a scour pit at the location of the sonar. Bedform asymmetry and height were estimated using Eqs. (7)–(9) assuming the seabed was flat. The resulting error in asymmetry as a function of  $\theta$  and  $\alpha$  is shown in Fig. 4c with the error in height as a function of  $\theta$  and aspect ratio,  $h/\lambda$ , shown in Fig. 4d.

TABLE 4. Coefficients of error function in estimated height for bedforms that are sinusoidal yet assumed triangular.

Coefficients	Estimate	Standard error
$\beta_0$	-0.2439	0.0004
$\beta_1$	0.3914	0.0009
$oldsymbol{eta}_2$	-0.1088	0.0004

An empirical model was fit to the error in asymmetry using linear regression. The model is described in Eq. (15) with an  $R^2$  of 0.89 and the coefficients (given in Table 5) are significant with a p value less than 0.001,

$$\alpha_{\text{est}} - \alpha = \beta_0 + \beta_1 \theta + \beta_2 \alpha + \beta_3 \theta \alpha. \tag{15}$$

A model was fit to the error in bedform height as a function of  $\theta$  with an  $R^2$  of 0.88 [Eq. (16)]. Coefficients are given in Table 6 and are all significant with a p value less than 0.001,

$$\frac{h_{\text{est}} - h}{h} = \beta_0 \frac{h}{\lambda} + \beta_1 \frac{h}{\lambda} \theta. \tag{16}$$

Equations (15) and (16) can be solved for  $\alpha$  and h, respectively, to correct for the error.

# c. Estimation of horizontal range

When the distance from the sonar and sonar-facing slope are such that all points on the slope are roughly at the same range, the horizontal range cannot be approximated as the depth independent range, and the elevation of the seabed relative to the sonar must be considered (Fig. 1). This can occur when the sonar is mounted at a height similar to that of the bedforms, or when a bedform has a slope perpendicular to the ray slope. In these cases the length of the high return may be very small relative to the actual horizontal length. This underestimation of brightness (B) and overestimation of shadow length (S) results in a smaller estimated value of c on both sides of the sonar, producing an underestimation (overestimation) of  $\alpha$  on the right (left) side [Eq. (7)]. The value of h is also overestimated on both sides when considering the under- and overestimation of c, S, and B [Eqs. (8) and (9)]. This should be considered when there are large bedforms present or bedforms on a sloped seabed such that the horizontal range cannot be approximated from the slant range and height of the sonar.

Given a theoretical field of triangular bedforms, and using the depth independent range as an approximation for the horizontal range, the errors are shown in Figs. 4e and 4f as a function of bedform aspect ratio  $(h/\lambda)$  for  $10^5$  configurations. The height estimate is strongly influenced by very asymmetric bedforms such that the height

TABLE 5. Coefficients corresponding to the empirical model in error in estimated asymmetry where scour at the location of the sonar causes a sloped seabed.

Coefficients	Estimate	Standard error
$egin{array}{c} eta_0 \ eta_1 \ eta \end{array}$	$5.13 \times 10^{-3}$ $-3.05 \times 10^{-3}$ $-1.02 \times 10^{-2}$	$1.98 \times 10^{-4}$ $1.15 \times 10^{-5}$ $3.50 \times 10^{-4}$
$eta_2 \ eta_3$	$6.09 \times 10^{-3}$	$2.02 \times 10^{-5}$

estimates can become negative or extremely large. Therefore, the asymmetry is varied from 0.05 to 0.95 to generate an empirical model of the true error. Linear theory for current-generated bedforms in equilibrium predict an asymmetry of 0.67 (or equivalently 0.33); therefore, excluding the asymmetries greater than 0.95 and smaller than 0.05 does not undermine the method or error model (Haque and Mahmood 1985).

An empirical model described by Eq. (17) was fit to the error in asymmetry. The model has an  $R^2$  of 0.78 and all coefficients are significant with a p value less than 0.001. The coefficients are shown in Table 7,

$$\alpha_{\text{est}} - \alpha = \beta_0 + \beta_1 \frac{h}{\lambda} + \beta_2 \alpha + \beta_3 \frac{h}{\lambda} \alpha.$$
 (17)

When estimating the height, the error can be represented by the empirical equation Eq. (18) with an  $R^2$  of 0.83. All coefficients are significant with a p value less than 0.001 and are shown in Table 8,

$$\frac{h_{\text{est}} - h}{h} = \beta_0 \frac{h}{\lambda} + \beta_1 \left(\frac{h}{\lambda}\right)^2 + \beta_2 \left(\frac{h}{\lambda}\right)^2 \frac{h}{H_i} + \beta_3 \left(\frac{h}{\lambda}\right)^2 \left(\frac{h}{H_i}\right)^2. \tag{18}$$

Similar to the other variations, the asymmetry and height estimates can be corrected by solving Eqs. (17) and (18) for  $\alpha$  and h, respectively. The aspect ratio  $h/\lambda$  can be approximated as the empirically corrected bedform height over the estimated wavelength when correcting for the asymmetry.

# d. All seabed configurations considered

It is possible to have a bedform configuration that contains a combination of rounded crests and troughs and a sloped seabed with unknown horizontal range. To account for this, the empirical corrections in the equations given above were applied to randomly generated seabed configurations that consist of sinusoidal bedforms on a scoured seabed where the horizontal range is approximated as depth independent. The error in computed asymmetry and height versus the true parameter is shown in Fig. 5 for both the original estimated values and the empirically corrected values.

TABLE 6. Empirical model coefficients for error in estimated height when a scoured seabed is considered.

Coefficients	Estimate	Standard error	
$\beta_0$	-0.068	0.003	
$oldsymbol{eta}_1$	0.055	0.000	

The error of the original asymmetry estimate has a mean of  $0.00 \pm 0.77$  (standard deviation) with 95% of the data contained in the interval [-0.06, 0.06]. The corrected asymmetry by applying the empirical model has a mean of  $0.00 \pm 0.20$  with a 95% confidence interval [-0.03, 0.03]. Similarly, the error in the original estimation of aspect ratio,  $h/\lambda$  has a mean of  $0.01 \pm 0.23$  with a 95% confidence interval [-0.05, 0.07]. The error for the empirically corrected aspect ratio is  $-0.01 \pm 0.22$  with 95% of the data constrained by the interval [-0.04, 0.02].

Overall, applying the empirical corrections in estimated height and asymmetry improves the estimates and better accounts for the actual bedform configuration and system geometry.

# e. Bedform parameter distributions

The sensitivity of the method to the assumption of uniform bedforms was addressed by theoretically prescribing distributions of bedform parameters.

The sensitivity of the method to small discrepancies between individual bedforms was first considered by imposing a distribution of bedform heights and wavelengths to a theoretical bedform field. The parameters and their variation were chosen based on those observed in bathymetric data of wave-orbital ripples taken at the Martha's Vineyard Coastal Observatory (MVCO). In these data there is a strong linear correlation,  $\rho = 0.8$ , between ripple height and wavelength with the ripple height increasing as the wavelength increases. Therefore, an aspect ratio of 0.11, the average aspect ratio at MVCO, was chosen to remain constant for each bedform. In the field data, the ripple heights and wavelengths were normally distributed. Therefore, for the theoretical data, the wavelength was prescribed a normal distribution given the mean, 0.44 m, and standard deviation, 0.13 m, of the wavelengths at MVCO. The ripple height was then computed given the aspect ratio of 0.11, which agrees well with the mean and standard deviation of the ripple height observed at MVCO. A sonar height was prescribed to be 1.15 m based on the ideal sonar height in Eq. (19). The extent of the sonar range was set to be 20 m, which is the sonar extent at MVCO and 100 transects were considered. Finally, the asymmetry was set to 0.5 as wave-orbital ripples are symmetric.

TABLE 7. Coefficients for error in estimated asymmetry by approximating the horizontal range as depth independent.

Coefficients	Estimate	Standard error
$\beta_0$	0.0079	0.0001
$\beta_1$	-0.1314	0.0008
$\beta_2$	-0.0160	0.0002
$\beta_3$	0.2646	0.0015

Given these prescribed normal distributions of bedform height and wavelength in individual ripples, the resulting distribution of wavelength was also normal, while the distribution of bedform height was positively skewed. The percent error in the median height was only 2.8%, the percent error in median wavelength was 1.4%, and the percent error in asymmetry was 0.15%. Therefore, with a sufficient number of bedforms, the error from discrepancies in individual bedforms was such that the central tendency of asymmetry, height, and wavelength agrees with the prescribed asymmetry, height, and wavelength.

The case of two scales of bedforms in which the smaller, secondary bedforms are superimposed on the larger, primary bedforms was also considered numerically. This situation can occur in nature with both tidal megaripples and wave-orbital ripples. On tidal megaripples, at the reversal of flow, incipient current ripples ( $\lambda \approx 1000 d_{50}$ , or  $\sim$ 20 cm) form on top of larger megaripples (Yalin 1964; Venditti et al. 2005; Traykovski 2012). On wave-orbital ripples, smaller ( $\sim$ 20 cm) ripples can form in the troughs of meter-scale relict ripples left from previous wave events (Traykovski 2007). When there are superimposed bedforms, the secondary bedforms cast small shadows that otherwise would have been a bright return from the larger bedforms. If the method is directly applied with these shadow patterns, then the error becomes large. It is therefore advised that the user applies a moving average filter, at least the wavelength of the smaller bedforms, to average over these smaller shadow patterns. This would result in a lower intensity in a region that otherwise should have been fully illuminated. Therefore, the threshold should be set so the filtered areas with small shadows are classified as bright.

The error of applying the method to superimposed bedforms was considered for bedforms with wavelength ratios ranging from 6 smaller bedforms superimposed on a larger bedform to 40 smaller bedforms superimposed on a larger bedform, with both bedforms having an aspect ratio of 0.1. In all cases the height of the larger bedforms was set to 0.4 m with a wavelength of 4 m. Additionally, the height of the sonar was 1.2 m, an asymmetry of 0.6, and a sonar extent of 20 m. Although the error was not linear with respect to a large-bedform-to-small-bedform-wavelength ratio, the height estimates were underestimated by 10%–15%,

TABLE 8. Empirical coefficients of the error in estimated height assuming seafloor perturbations are significantly smaller than the height of the sonar when estimating the horizontal range.

Coefficients	Estimate	Standard error
$\beta_0$	-0.031	0.005
$\beta_1$	5.538	0.038
$\beta_2$	-14.196	0.116
$\beta_3$	9.352	0.132

with errors as large as 25%. The wavelength estimates were all overpredicted with a percent error ranging from 2% to 2.5%. Finally, the percent error in asymmetry was underestimated for all cases with an error of approximately 3%. Therefore, when superimposed bedforms are present, it is recommended to filter out the shadows from the smaller bedforms to obtain estimates of the larger bedforms. Estimating the smaller bedform height and asymmetry is more difficult, as they are generally superimposed on the steep lee and stoss sides of the primary bedforms.

As the superimposed bedform size becomes a significant fraction of the primary bedform size (e.g., three to four small bedforms per large bedform), filtering out the shadows becomes impractical and the technique produces large errors. However, as the secondary bedforms become too large to successfully filter their shadows, the bedform field becomes similar to the case of variation in bedform parameters on a flat bed. For secondary bedforms that are a factor of 2 smaller than the primary bedforms, which is close to the worst-case scenario, the error in height is 37% and an error in asymmetry of 10%.

#### 4. Method

### a. Instrument configuration

This method relies on data collected from a lowmounted sonar such that shadows exist. To provide better statistical estimates of height and asymmetry, it is recommended that the sonar is mounted such that there is a sufficient number of bedforms with shadows and that the lengths of the shadows are not significantly large compared to the bright return. There is a trade-off between these two criteria, as a very low mounted sonar will produce a large number of bedforms with shadows; however, most of the domain will be shadows with the bright regions very small, leading to errors in estimating S/(BL). We recommend that at least 80% of the bedforms in the domain cast shadows and that at the midpoint of this shadowed region the brightness length is 30% of the bedform wavelength (Fig. 3a shown by the  $0.2x_{\text{sonar}}$  and  $0.3\lambda$  annotations). Additionally, if the

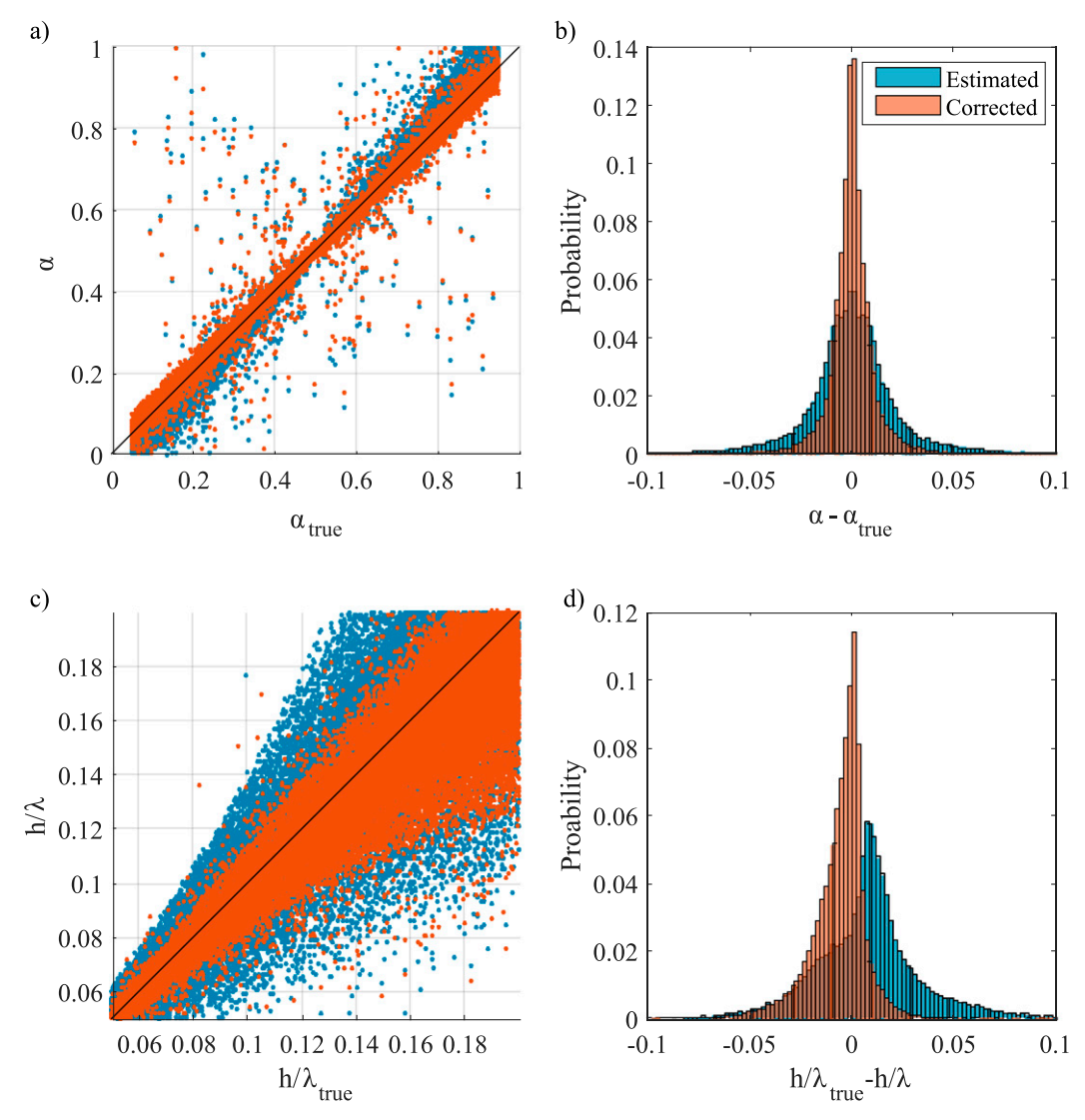


FIG. 5. (a) Estimated asymmetry vs true asymmetry for theoretical bedforms when sinusoidal bedforms on a slanted seabed with an depth independent estimated horizontal range are considered together. Data from assuming triangular bedforms on a flat seabed with horizontal range (blue) and data empirically corrected (red). A perfect fit is shown (black line). (b) Probability of the error in asymmetry for both estimated and empirically corrected asymmetry. (c) Estimated  $h/\lambda$  vs true  $h/\lambda$  when all variations are considered. (d) Probability of the error in height.

bedforms are sinusoidal, the critical length,  $x_{\rm crit}$  described in section 3a would ideally be located at the midpoint of the shadowed bedforms (Fig. 3a).

The ideal sonar height from the seabed,  $H_i$ , is analytically determined for the three criteria mentioned above given the system geometry and assuming symmetric triangular bedforms,

$$H_i = \gamma \frac{h}{\lambda} x_{\text{sonar}} + \frac{h}{\lambda} \lambda \,, \tag{19}$$

where  $\gamma$  varies for each criterion and is shown in Table 9. Given these values of  $\gamma$ , it is recommended that users set

 $\gamma=0.6$ , as the frame on which the sonar is mounted will typically settle a few centimeters, resulting in a final  $\gamma=0.5$ . Additionally, while  $h/\lambda$  may be unknown prior to deploying the instrument, typical values are usually 0.1–0.15 for wave orbital ripples and 0.05–0.1 for current-generated megaripples, which can be used as an initial approximation in Eq. (19) (Ashley 1990; Nielsen 1992).

# b. Data analysis steps

1) Transform the rotary side-scan sonar imagery into x-y coordinates using the approximation for horizontal range given in Eq. (2).

TABLE 9. Analytical coefficients for recommended sonar height from the seabed.

Criteria	γ
80% of bedforms contain shadows	< 0.51
30% of bedform wavelength is illuminated at	>0.55
the midpoint of the shadowed region	
$x_{\rm crit}$ occurs at the midpoint of the shadowed region	0.4

- Determine the orientation of the bedforms using either a 2D fast Fourier transform or variability analysis (Van Dijk and Lindenbergh 2017; Pluymaekers et al. 2007).
- Take transects of the backscatter intensity perpendicular to the bedform crest.
- 4) Remove the background attenuated echo return strength caused by beam spreading and attenuation.
- 5) If secondary bedforms exist on primary bedforms, filter out the secondary bedform shadows.
- 6) Empirically identify a threshold intensity to distinguish between shadows and bright regions.
- Compute the distance to the start of each shadow (L), the length of the shadow (S), the wavelength (λ), and the length of the bright region (B, from the wavelength and shadow length).
- 8) Calculate *S*/(*BL*) for each bedform and on each side of the sonar.
- 9) Plot a histogram of S/(BL) for each side and determine what central tendency best represents the distribution.
- 10) Use Eq. (7) to calculate the asymmetry,  $\alpha$ , assuming triangular bedforms and using the central tendency of S/(BL) for each side as obtained in step 9.
- 11) Estimate the height for each bedform using Eqs. (8) and (9) for each side where  $\alpha$  is obtained in step 10 and the values of S, B, L, and  $\lambda$  exist for each bedform.
- 12) Plot a histogram of  $h_r$  and  $h_l$ , and determine what central tendency best represents the distribution.
- 13) Apply corrections for crest sharpness, scoured seabed, and horizontal range using Eqs. (13)–(18), if needed.

### 5. Validation from field data

The method is validated against wave-orbital ripples and tidally reversing megaripples in which both a rotary sidescan sonar and bathymetric-measuring instruments were deployed. The operating parameters of the different sonars are listed in Table 10. The bathymetric data are obtained directly below the quadpod and the rotary sidescan sonar images up to 20 m away from the quadpod. While some variations in bedform geometry may occur directly under the quadpod given the interaction of the frame with the flow and an erodible seabed, the bedforms are considered to be similar, permitting the bathymetric instruments to provide ground truth for the method.

# a. Wave-orbital ripples

Bedform height and asymmetry were estimated on wave-orbital ripples located in 8-m-deep water approximately 1.3 km shoreward from the MVCO offshore node, an observatory roughly 1.5 km offshore of the southern coast of Martha's Vineyard. The location is dominated by waves with little-to-no influence of tidal currents. The data were collected in 2007 using a quadpod equipped with both a rotary sidescan sonar and a two-axis pencil beam sonar similar to a dataset collected in 2005 and documented in Traykovski (2007) that was also located at MVCO in 12-m water depth. The sidescan sonar, deployed 1.67 m from the seabed, captured the backscatter intensity over a radius of 20 m around the quadpod, and the pencil beam sonar obtained bathymetric data over a 2 m × 2 m region directly beneath the quadpod (Fig. 6a).

Ripple height and asymmetry were estimated over a 24-day period from the rotary sidescan sonar and compared to the same parameters obtained from the pencil beam sonar (Fig. 7). The height, asymmetry, and wavelength for each bedform were estimated using the method described above for the rotary sidescan sonar. These parameters were computed using a zero-crossing

TABLE 10. Operating parameters of sonars used in field validation of the method.

Instrument	881L rotary sidescan sonar		881A two-axis pencil beam sonar	DT100 multibeam profiling sonar
Location	MVCO	Columbia River mouth	MVCO	Columbia
Elevation (m)	1.67	1.10	1.00	2.80
Frequency (kHz)		675	1100	675
Range (m)		20	4	20
Range resolution (m)		0.04	0.008	0.04
Pulse length (μs)		20	10	52
Step size (°)		0.3	1.2	0:162, 3° between beams
Azimuth step size (°)		_	1.6	3
Transducer beamwidth (°)		$1.8 \times 20$	1.3	$120 \times 3$
Averaging	4	sequential scans	None	8 pings in each azimuth step

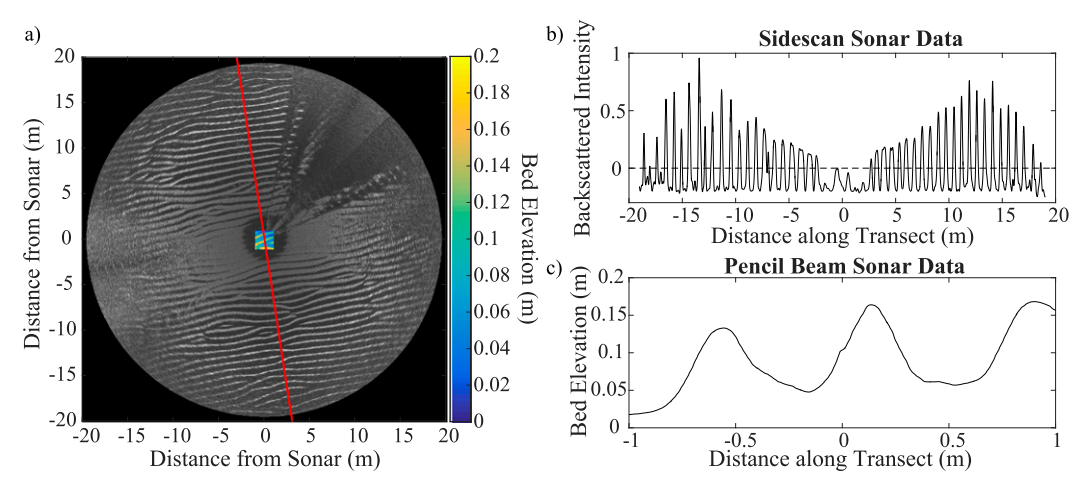


FIG. 6. (a) Rotary sidescan sonar (grayscale) and pencil beam sonar (overlaid color) data of wave-orbital ripples taken at 1700:00 UTC 5 Oct 2007 off the southern coast of Martha's Vineyard. An arbitrary transect taken perpendicular to the ripple crests (red line). (b) Backscatter intensity of sidescan sonar data taken along the transect. The threshold used to distinguish shadow and bright regions in the method (dashed line). (c) Bed elevation from a transect along the pencil beam sonar data. The bed elevation is relative to the lowest elevation in the survey area.

method on the pencil beam data, in which the wavelength was defined as the distance between two troughs, the height was the averaged distance from peak to each trough, and the asymmetry was the horizontal distance from the location of the peak to the trough divided by the wavelength (Fig. 6c).

For each time step, the median bedform height, wavelength, aspect ratio  $(h/\lambda)$ , and asymmetry were computed from the bedforms on multiple parallel transects (Fig. 7). The median was used as the measure of central tendency because it is more robust than the mean to skewed distributions and outliers. A 95% confidence interval for the median was computed for bedform height, wavelength, and aspect ratio assuming the median is binomially distributed around the estimated value (Rice 2002). The 95% confidence interval for the bedform asymmetry was computed using a 1000-sample bootstrap method, given the interaction of terms in computing the asymmetry parameter. These 95% confidence intervals are represented by the shaded regions in Fig. 7.

Estimates of bedform parameters from the sidescan sonar show good agreement with the computed parameters from the pencil beam sonar (Fig. 7). The mean absolute difference in asymmetry between the two instruments is  $0.019 \pm 0.021$  (standard deviation) with the mean absolute difference in height of  $0.017 \, \text{m} \pm 0.016 \, \text{m}$ , which corresponds to a mean percent error of  $34.0\% \pm 27.2\%$ .

The asymmetry ( $\alpha$ ) is approximately 0.5 throughout the entire time series, which is consistent with literature on wave-orbital ripples (Bagnold 1946; Traykovski et al. 1999). While the estimated asymmetry agrees well with

the bathymetric data, the sidescan sonar data tend to overestimate ripple height and wavelength compared to the pencil beam sonar. This discrepancy could be due to the effect of the frame on the seabed and the flow, as the pencil beam sonar measures approximately three bedforms directly below the sonar, and the rotary sidescan sonar (with the shadow method) relies on bedforms 4-20 m from the quadpod. The estimated wavelength and bedform height were plotted with respect to distance from the sonar to determine how these parameters vary with distance from the sonar. These plots revealed that the wavelengths linearly increased with distance from the sonar. Although the bedform height increased with distance from the sonar during some periods, it decreased during others. To better compare the estimated parameters with that from the pencil beam sonar taken directly below the sonar, a linear regression was fit to the data to predict the bedform parameters under the frame as a function of the distance from the sonar. The estimates from the rotary sidescan sonar were then linearly extrapolated to provide an estimate of their values directly under the frame (Fig. 7). This extrapolated value accounts for some of the overestimation in bedform wavelength and is also able to capture the sudden decrease in wavelength around 6 October 2007. Studies on the effect of frames on the seabed and flow have shown that in the presence of waves, there is increased turbulence near the frame (Bolaños et al. 2011; Williams et al. 2003). While the results of Bolaños et al. (2011) and Williams et al. (2003) indicate that the frame does not have as large of an effect on the flow and seabed in

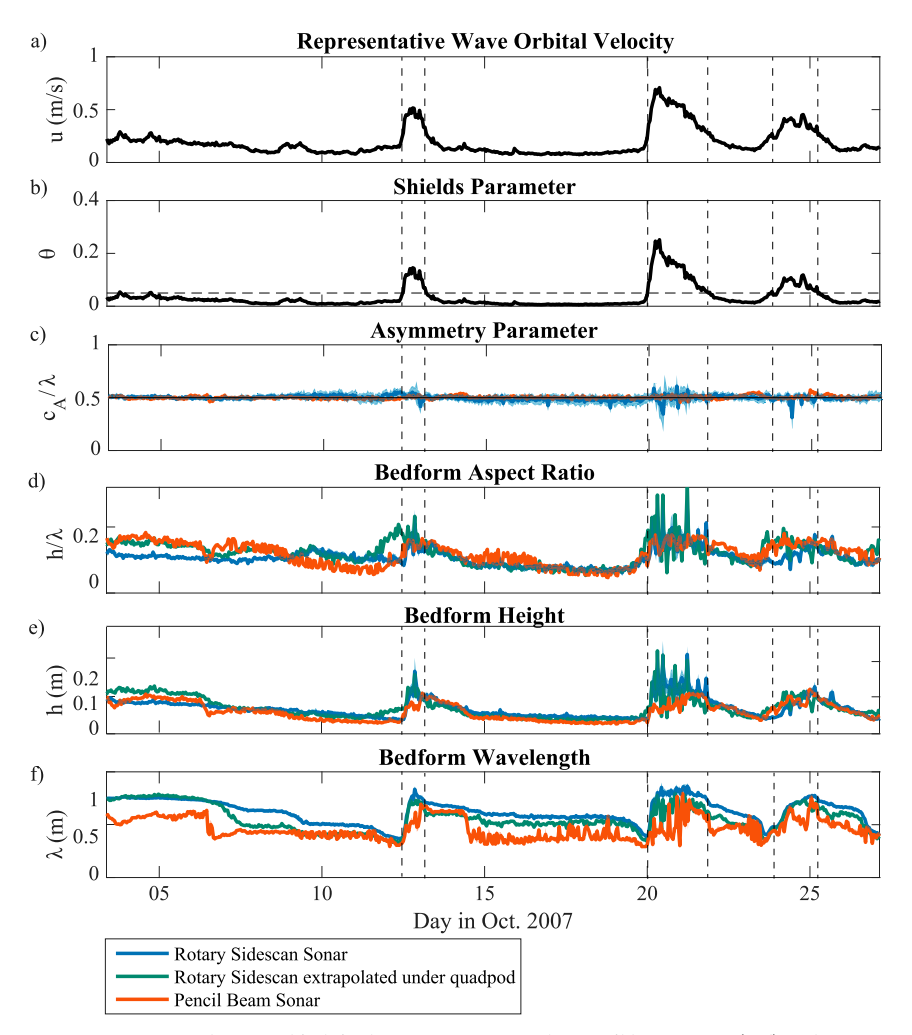


FIG. 7. Computed wave-orbital ripple parameters from the pencil beam sonar (red) and rotary side-scan sonar (blue) over a 24-day period for bedforms located at MVCO. The 95% confidence intervals of the parameters (shaded regions). The estimation of the bedform parameters directly below the sonar obtained from extrapolating the data from the rotary side-scan sonar (green). (a) Representative wave-orbital velocity from an acoustic Doppler velocimeter (ADV) located on a nearby quadpod. (b) Computed Shields parameter. The critical Shields parameter is marked (dashed line at 0.05). (c) Estimated bedform asymmetry. (d) Bedform aspect ratio has good agreement between the estimates from the rotary sidescan sonar and the pencil beam sonar. (e) Bedform height, which show an increase in height during large wave events. (f) Bedform wavelength. The overestimation of wavelength from the rotary sidescan sonar could result from the influence of the quadpod on the surrounding flows and seabed.

wave conditions as opposed to strong currents, it is hypothesized that this increased turbulence can result in the bedforms under the frame adjusting to a new equilibrium configuration faster than the bedforms away from the frame.

While height and bedform aspect ratio  $(h/\lambda)$  estimates agree well during the waning stages of the wave events, there is noise and disagreement in the estimates at the onset and peak stages. A large part of this disagreement is due to the noise in the data from both sonars. During high wave events, suspended sediment obscures

the seabed, resulting in noise in the estimates and little confidence in their estimates. Overall, the method is able to capture the changes in bedform parameters that span multiple large wave events with some of the error being attributed to the assumption of coincident observation areas as well as noise during periods of high suspended sediment.

### b. Tidally reversing megaripples

The method was further tested on tidally reversing megaripples located at the mouth of the Columbia River,

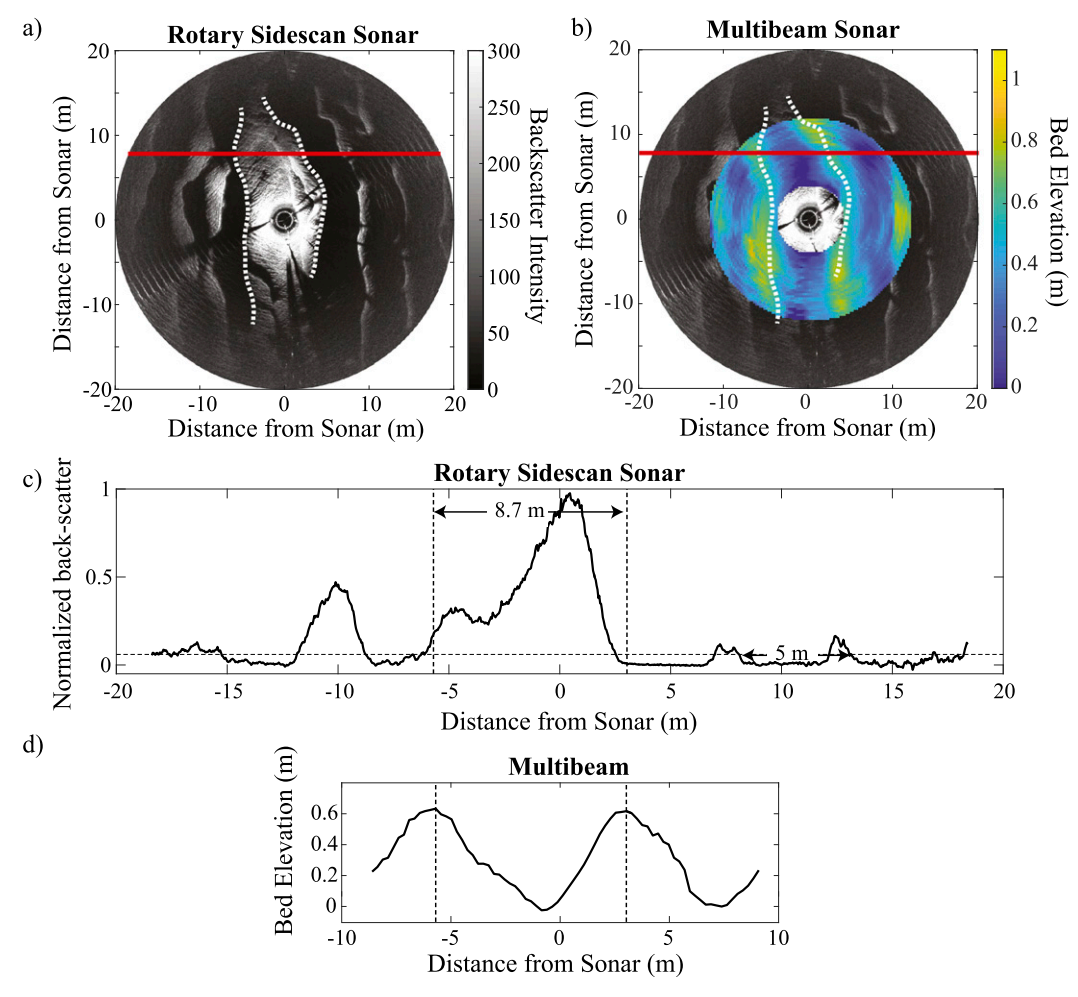


FIG. 8. (a) Rotary sidescan sonar data of megaripples taken at 1743:18 UTC 10 May 2013 at the mouth of the Columbia River. An arbitrary transect taken perpendicular to the bedform crests is marked (red line). The start of a shadow region closest to the sonar (white dashed lines). (b) Multibeam data taken at the same time as the rotary sidescan sonar. The white dashed lines are superimposed at the same location on the multibeam data to show agreement in bedform detection from both instruments. (c) Backscatter intensity of sidescan sonar data taken along the transect. The threshold used to distinguish shadow and bright regions in the method (horizontal dashed line) is marked as is the location of the crests in the multibeam data (vertical dashed lines). (d) Bed elevation from a transect along the multibeam sonar data. The bed elevation is relative to the lowest elevation in the survey area.

which discharges into the Pacific Ocean between Washington and Oregon. This location has large tidally reversing megaripples that change orientation and migration direction with the tides. Traykovski (2015) deployed a quadpod equipped with a rotary sidescan sonar as well as a side-looking multibeam rotary sonar (Figs. 8a,b). The rotary sidescan sonar, located 1.1 m from the seabed, obtained an image of the seabed up to a range of 20 m while the multibeam rotary sonar observed the bathymetry of the seabed within a 12-m radius.

Bedform asymmetry and height were estimated from the multibeam sonar by detecting bedform peaks and troughs in transects perpendicular to the bedform orientation (Fig. 8c). Asymmetry was estimated by dividing c by the wavelength, and bedform height was estimated by subtracting the height of the crest from the average height of the trough on each side of the crest. Again, the median was used as the measure of central tendency, and 95% confidence intervals were obtained from a binomial distribution for the height, wavelength, and aspect ratio with a 1000-sample bootstrap being used to compute the confidence interval for the asymmetry (Rice 2002).

The asymmetry of the bedforms from the multibeam sonar was then compared to the estimated asymmetry from the rotary sidescan sonar (Fig. 9). There is less confidence in the estimates for the Columbia River than for MVCO, as there are significantly fewer bedforms in the domain and the bedforms are not as uniform

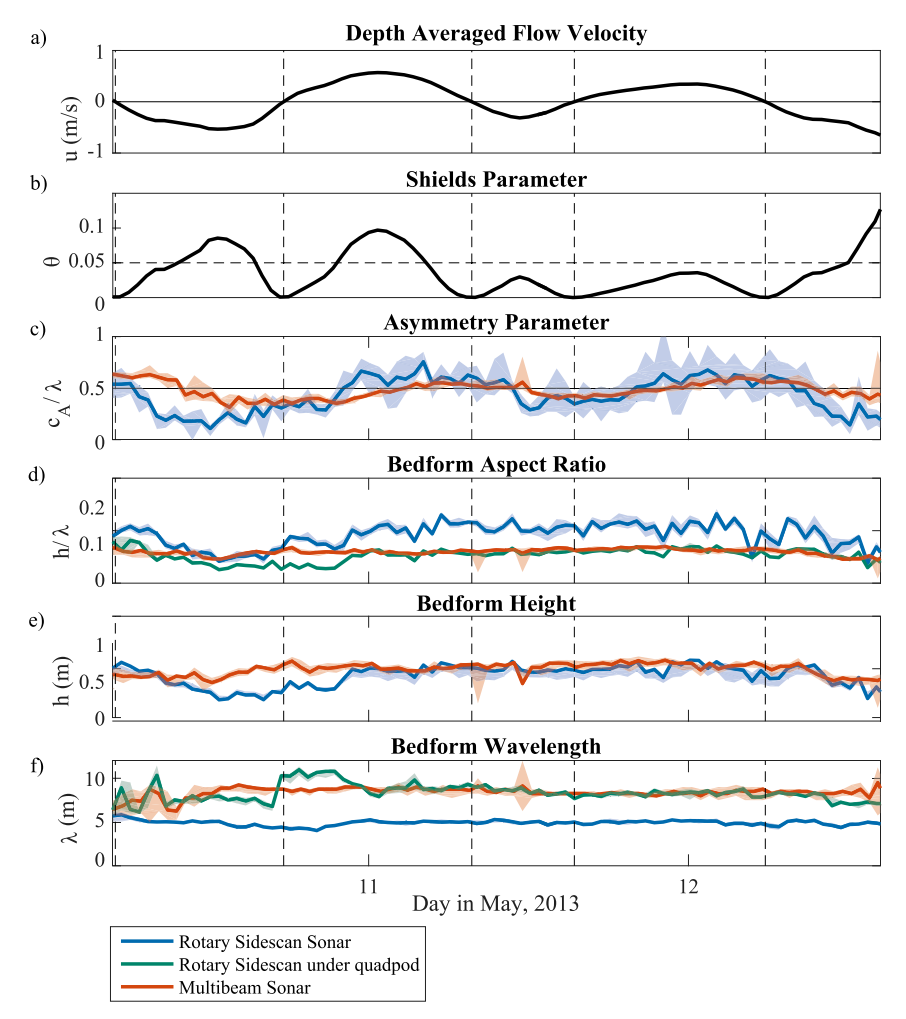


FIG. 9. Computed megaripple parameters from the multibeam sonar (red) and rotary side-scan sonar (blue) over a 2.5-day period for bedforms located at the mouth of the Columbia River. The estimation of the bedform parameters directly below the quadpod (green). The 95% confidence intervals of the parameters (shaded regions). (a) The depth-averaged flow obtained from the same quadpod as the rotary side-scan sonar. (b) Computed Shields parameter with the critical Shields parameter indicated (dashed black line). (c) Estimated bedform asymmetry. (d) Bedform aspect ratio  $(h/\lambda)$  that is overestimated for the rotary sidescan sonar given the underestimation of wavelength; however, when only the bedform wavelength directly below the quadpod is considered, there is good agreement. (e) Bedform height that is in good agreement between the two instruments. (f) Bedform wavelength in which the bedforms closest to the sonar have a larger wavelength than those farther from the sonar.

given their two-dimensionality in plan view. This two-dimensionality is partly due to the megaripples bifurcating, which add to the noise in the data. The method captures the tidal reversal of the bedforms given the asymmetry and accurately measures the bedform height; however, there are large discrepancies in wavelength and therefore aspect ratio. The almost factor-of-2 difference in wavelength is due to the fact that the multibeam is surveying the bedforms directly under the quadpod, where the wavelengths are larger, while the method considers bedforms far from the frame

where shadows are produced and the wavelengths are smaller. The wavelength of the rotary sidescan sonar was computed beneath the frame for the period considered, which shows good agreement in wavelength and aspect ratio with the multibeam sonar (Figs. 9d,f). The difference in bedform wavelength in the presence of the frame is hypothesized to be attributed to current-frame interactions. Bolaños et al. (2011) found that underwater frames increase the horizontal velocity under the frame, resulting in a scour pit. Because the megaripple wavelengths are on the same order of size as the

frame, it is believed this scour pit alters the bedform morphodynamics such that the wavelengths of bedforms under the frame are larger than those away from the frame.

While the height is accurately estimated most of the time, there is disagreement a few hours before 11 May 2013. During this time, many of the bedforms bifurcated, split, and later merged back together. This results in significant changes in the estimates from both the rotary sidescan sonar and the multibeam given the area each instrument surveyed. The lack of periodicity and three-dimensionality of the bedforms at the Columbia River add noise and uncertainty to the method. Overall, the mean absolute difference in asymmetry between the two instruments is  $0.11 \pm 0.10$  (standard deviation) with an absolute difference in height of  $0.08 \, \mathrm{m} \pm 0.07 \, \mathrm{m}$  that corresponds to an absolute percent error of  $16.6\% \pm 14.7\%$ .

#### 6. Conclusions

A method is outlined to estimate the height and asymmetry of bedforms from a low-mounted sidescan sonar that results in the formation of shadows in the back-scattered intensity data. The estimated heights and asymmetry agree moderately well with bathymetry data when applied to both wave-orbital ripples and tidally reversing megaripples given that bathymetric measurements were taken with much smaller and sometimes different sampling areas than the sidescan sonar measurements.

While this method of estimating bedform parameters was developed based on a uniform bedform distribution, it is reasonably tolerant of small variations in bedform height and wavelength. When there are small bedforms superimposed on larger bedforms, it is recommended that the shadows formed from the smaller bedforms are filtered out in order to estimate the larger bedform parameters. This procedure was tested with idealized numerical data and shows errors of around 10%–15% in height and 3% in asymmetry.

Although idealized cases provide unbiased estimates of asymmetry and height, some bias may exist in field data. Because the ground-truth bedforms from the field are not the same bedforms that are in the field of view of the rotary sidescan sonar, we do not have a way to test this bias in field data. We recommend studying this as future work where we can deploy a rotary sidescan sonar on a quadpod and take collocated surveys with a shipmounted multibeam sonar, or other larger sampling area techniques with high precision, to have the actual height distribution for all bedforms in consideration.

While this method is described for the deployment of a rotary sidescan sonar, it can be applied to other sidescan sonar systems, such as fixed on a frame or ship mounted, if the geometry from the sonar to the seabed and orientation of the bedforms is known. In the case of a fixed sidescan transducer mounted on a frame, the transducer should be mounted perpendicular to the bedform crests to obtain a single transect of the shadow pattern. Users can then begin the data analysis steps as described in section 4b at step 4. Future work could be taken to modify the method for ship-mounted sidescan sonars.

The addition of height and asymmetry information to the well-documented planform geometry data provided by sidescan sonars has the potential to increase the usefulness of such systems in studying the dynamics and properties of bedforms. The high temporal and spatial resolution of an imaging rotary sidescan sonar along with its relatively low costs make rotary sidescan sonars ideal instruments for imaging the seabed in shallow and energetic environments. Utilizing the shadows to provide estimates of bedform height and asymmetry will expand the capabilities of rotary sidescan sonars.

Acknowledgments. We acknowledge Jay Sisson, Andy Girard, and others in collecting the datasets that made this work possible. We thank Benjamin Jones, Bryce Corlett, and Jenny Wehof for their help throughout the method development process.

This project is partially supported by the National Science Foundation through a Graduate Research Fellowship and a Massachusetts Institute of Technology Energy Initiative Fellowship. Additionally, funding used in developing the method was obtained from NSF Grants OCE-1634481 and OCE-1635151. Field work was funded under ONR Grants N00014-06-10329 and N00014-13-1-0364.

### REFERENCES

Ashley, G. M., 1990: Classification of large-scale subaqueous bedforms; a new look at an old problem. *J. Sediment. Res.*, **60**, 160–172, https://doi.org/10.2110/jsr.60.160.

Bagnold, R. A., 1946: Motion of waves in shallow water. Interaction between waves and sand bottoms. *Proc. Roy. Soc. London*, 187A, 1–18, https://doi.org/10.1098/rspa.1946.0062.

Blondel, P., 2009: *The Handbook of Sidescan Sonar*. Springer-Verlag, 324 pp., https://doi.org/10.1007/978-3-540-49886-5.

Bolaños, R., L. O. Amoudry, and K. Doyle, 2011: Effects of instrumented bottom tripods on process measurements. J. Atmos. Oceanic Technol., 28, 827–837, https://doi.org/10.1175/2010JTECHO816.1.

Bouma, A. H., M. L. Rappeport, R. C. Orlando, and M. A. Hampton, 1980: Identification of bedforms in lower Cook Inlet, Alaska. Sediment. Geol., 26, 157–177, https://doi.org/ 10.1016/0037-0738(80)90010-X.

Chew, A. L., P. B. Tong, and C. S. Chia, 2007: Automatic detection and classification of man-made targets in side scan sonar images. 2007 Symposium on Underwater Technology and Workshop on Scientific Use of Submarine Cables and

- Related Technologies, IEEE, 126–132, https://doi.org/10.1109/UT.2007.370841.
- Clifton, H. E., and J. R. Dingler, 1984: Wave-formed structures and paleoenvironmental reconstruction. *Mar. Geol.*, **60**, 165–198, https://doi.org/10.1016/0025-3227(84)90149-X.
- Coiras, E., Y. Petillot, and D. M. Lane, 2007: Multiresolution 3-D reconstruction from side-scan sonar images. *IEEE Trans. Image Process.*, **16**, 382–390, https://doi.org/10.1109/TIP.2006.888337.
- Dalrymple, R. W., and R. N. Rhodes, 1995: Estuarine dunes and bars. *Developments in Sedimentology*, Elsevier, 359–422, https://doi.org/10.1016/S0070-4571(05)80033-0.
- Doherty, M. F., J. G. Landowski, P. F. Maynard, G. T. Uber, D. W. Fries, and F. H. Maltz, 1989: Side scan sonar object classification algorithms. Proceedings of the Sixth International Symposium on Unmanned Untethered Submersible Technology, IEEE, 417-424, https://doi.org/ 10.1109/UUST.1989.754734.
- Green, M. O., 1986: Side-scan sonar mosaic of a sand ridge field: Southern Mid-Atlantic Bight. Geo-Mar. Lett., 6, 35–40, https://doi.org/10.1007/BF02311694.
- Haque, M. I., and K. Mahmood, 1985: Geometry of ripples and dunes. J. Hydraul. Eng., 111, 48–63, https://doi.org/10.1061/ (ASCE)0733-9429(1985)111:1(48).
- Hay, A., and D. Wilson, 1994: Rotary sidescan images of nearshore bedform evolution during a storm. *Mar. Geol.*, **119**, 57–65, https://doi.org/10.1016/0025-3227(94)90140-6.
- Irish, J., J. Lynch, P. Traykovski, A. Newhall, and K. Prada, 1999: A self-contained sector-scanning sonar for bottom roughness observations as part of sediment transport studies. *J. Atmos. Oceanic Technol.*, 16, 1830–1841, https://doi.org/10.1175/1520-0426(1999)016<1830:ASCSSS>2.0.CO;2.
- Klein, M., 2002: Side scan sonar. *International Handbook of Underwater Archaeology*, C. V. Ruppé and J. F. Barstad, Eds., Springer Series in Underwater Archaeology, Springer, 667–678, https://doi.org/10.1007/978-1-4615-0535-8\_39.
- Lefebvre, A., A. J. Paarlberg, and C. Winter, 2016: Characterising natural bedform morphology and its influence on flow. *Geo-Mar. Lett.*, 36, 379–393, https://doi.org/10.1007/ s00367-016-0455-5.
- Lonsdale, P., W. R. Normark, and W. A. Newman, 1972: Sedimentation and erosion on Horizon Guyot. *Geol. Soc. Amer. Bull.*, 83, 289–316, https://doi.org/10.1130/0016-7606(1972)83[289:SAEOHG]2.0.CO;2.
- Nelson, J. M., S. R. McLean, and S. R. Wolfe, 1993: Mean flow and turbulence fields over two-dimensional bed forms. Water Resour. Res., 29, 3935–3953, https://doi.org/10.1029/93WR01932
- Nielsen, P., 1992: Coastal Bottom Boundary Layers and Sediment Transport. Advanced Series on Ocean Engineering, Vol. 4, World Scientific, 340 pp.
- Nishimura, C. E., 1997: Fundamentals of acoustic backscatter imagery. Naval Research Laboratory Tech. Rep. NRL/FR/7420-97-9848, 71 pp.

- Pluymaekers, S., R. Lindenbergh, D. Simons, and J. de Ronde, 2007: A deformation analysis of a dynamic estuary using twoweekly MBES surveying. OCEANS 2007—Europe, Aberdeen, United Kindom, IEEE, 6, https://doi.org/10.1109/ OCEANSE.2007.4302305.
- Reed, S., Y. Petillot, and J. Bell, 2003: An automatic approach to the detection and extraction of mine features in sidescan sonar. *IEEE J. Oceanic Eng.*, **28**, 90–105, https://doi.org/10.1109/JOE.2002.808199.
- Rice, J. A., 2002: *Mathematical Statistics and Data Analysis*. 2nd ed. Duxbury Press, 602 pp.
- Rubin, D., D. McCulloch, and H. Hill, 1983: Sea-floor-mounted rotating side-scan sonar for making time-lapse sonographs. *Cont. Shelf Res.*, **1**, 295–301, https://doi.org/10.1016/0278-4343(83)90029-8.
- Smith, J. D., and S. R. McLean, 1977: Spatially averaged flow over a wavy surface. J. Geophys. Res., 82, 1735–1746, https://doi.org/ 10.1029/JC082i012p01735.
- Tang, D., K. L. Williams, and E. I. Thorsos, 2009: Utilizing high-frequency acoustic backscatter to estimate bottom sand ripple parameters. *IEEE J. Oceanic Eng.*, 34, 431–443, https://doi.org/10.1109/JOE.2009.2015402.
- Traykovski, P., 2007: Observations of wave orbital scale ripples and a nonequilibrium time-dependent model. *J. Geophys. Res.*, **112**, C06026, https://doi.org/10.1029/2006JC003811.
- ——, 2012: SW (new) channel rotary sidescan imagery of bedforms in New River Inlet, NC. Vimeo video, 3:40, from the Imagenex 881L rotary sidescan sonar on Traykovski's Quadpod 20 m north-west of the #4 Red Channel marker, https://vimeo.com/ 44806773.
- —, 2015: Observations of the geometry and migration of tidally reversing dunes. *Coastal Sediments 2015: The Proceedings of the Coastal Sediments 2015*, P. Wang, J. D. Rosati, and J. Cheng, Eds., World Scientific, 8–14, https://doi.org/10.1142/9789814689977 0126.
- —, A. E. Hay, J. D. Irish, and J. F. Lynch, 1999: Geometry, migration, and evolution of wave orbital ripples at LEO-15.
  J. Geophys. Res., 104, 1505–1524, https://doi.org/10.1029/1998JC900026.
- Van Dijk, T. A. G. P., and R. C. Lindenbergh, 2017: Methods for analysing bedform geometry and dynamics. *Atlas of Bedforms* in the Western Mediterranean, J. Guillén et al., Eds., Springer, 7–13, https://doi.org/10.1007/978-3-319-33940-5\_2.
- Venditti, J. G., M. Church, and S. J. Bennett, 2005: Morphodynamics of small-scale superimposed sand waves over migrating dune bed forms. Water Resour. Res., 41, https://doi.org/ 10.1029/2004WR003461.
- Williams, J., P. Bell, L. Coates, N. Metje, and R. Selwyn, 2003: Interactions between a benthic tripod and waves on a sandy bed. *Cont. Shelf Res.*, 23, 355–375, https://doi.org/10.1016/ S0278-4343(02)00188-7.
- Yalin, M. S., 1964: Geometrical properties of sand waves. *J. Hydraul. Eng.*, **90**, 105–119.